High-stress creep preceding coseismic rupturing in amphibolite-facies ultramylonites

Simone Papa[a], Giorgio Pennacchioni[a], Luca Menegon[b,c], and Marcel Thielmann[d]

[a]*Department of Geosciences, University of Padova, Via Gradenigo 6, I-35131 Padua, Italy*

[b]*School of Geography, Earth and Environmental Sciences, University of Plymouth, Drake Circus, PL48AA Plymouth, UK*

[c]*The Njord Centre, Department of Geosciences, University of Oslo, Postbox 1048, Blindern, 0316 Oslo, Norway*

[d]*Bayerisches Geoinstitut, University of Bayreuth, Universitätstraße 30, 95440 Bayreuth, Germany*

Corresponding author: simone.papa@phd.unipd.it - simonepapa.geo@gmail.com

Abstract

Coeval pseudotachylytes (solidified melts produced during seismic slip) and mylonites are generally regarded as the geological record of transient seismic events during dominant ductile flow. Thermal runaway has been proposed as a model to explain the pseudotachylyte-mylonite association. In the Mont Mary unit (Western Alps), pseudotachylyte fault veins occur along the amphibolite-facies (ca. 550 °C; 0.35 GPa) ultramylonitic foliation of paragneisses. These veins formed at the same metamorphic conditions of the ultramylonites, thus potentially recording thermal runaway. We analysed the microstructure of quartz in ultramylonite and of ultramylonite clasts in pseudotachylyte to investigate the possible occurrence of thermal runaway. Quartz aggregates show an evolution under constant temperature to ultrafine-grained recrystallised grain size (2.5 μm), reflecting creep under high differential stresses (> 200 MPa) and high strain rates (10^{-9} s^{-1}), along very narrow foliation-parallel layers. In the ultrafine aggregates, viscous grain boundary sliding became dominant and promoted cavitation leading to disintegration of quartz aggregates and precipitation, in the pore space, of biotite, oriented parallel to the main ultramylonitic foliation. The strain rate-limiting process was aseismic fluid-assisted precipitation of biotite. The potential occurrence, at the deformation conditions of the Mont Mary ultramylonites, of thermal runaway in pure quartz layers was investigated by numerical modelling. The models predict a switch from stable flow to thermal runaway at background strain rates faster than 10^{-9} s^{-1} for critical differential stresses that are comparable to the brittle strength of rocks. Deformation of ultramylonites occurred close to the conditions for thermal runaway to occur, but based on the microstructural record we conclude that the Mont Mary pseudotachylyte-mylonite association is best explained by brittle failure, triggered by transients of high differential stress and strain rate causing a downward deflection of the brittle-ductile transition.

Keywords: pseudotachylyte; EBSD; brittle-ductile transition; lower crustal earthquake; quartz rheology; thermal runaway.

1. Introduction

Pseudotachylyte is a solidified melt produced during seismic slip along a fault in silicate rocks. Coeval pseudotachylytes and mylonites in exhumed mid to lower crustal rocks record transient seismic slip during ductile flow (e.g. Sibson, 1980). Different models have been proposed to explain this association of fault rocks. Earthquake ruptures nucleating at the base of the seismogenic crust can propagate downward into the underlying ductile crust (Tse and Rice, 1986) producing pseudotachylytes that are then overprinted by mylonitisation during post- and inter- seismic creep. Numerical models show that seismic faulting in the upper crust can cause a transient downward deflection of the brittle-ductile transition and a zone of increased strain rate below the fault tip (Ellis and Stöckhert, 2004). This can explain transient high differential stresses in the middle to lower crust resulting in aftershock seismicity in the otherwise ductile crust (e.g. Cheng and Ben-Zion, 2019; Jamtveit et al., 2018).

The above process requires an external trigger for the mid-lower crustal seismicity. Alternatively, a local trigger for seismicity may be associated with stress amplification due to strain incompatibility of jostling rigid blocks bounded by a network of intersecting ductile shear zones (Hawemann et al., 2019; Campbell et al., 2020). Where deep-seated pseudotachylytes are not associated with mylonites, a local trigger for seismicity may be represented by the release of high long-term differential stresses accumulated in dry metastable rocks due to brittle fracturing (e.g. Scambelluri et al., 2017).

Hobbs et al. (1986) proposed that pseudotachylytes could nucleate during high temperature flow due to ductile instability. Such instabilities develop as result of extreme weakening due to the positive feedback between shear heating and viscosity, a process known as thermal runaway. Numerical models (e.g. Kelemen and Hirth, 2007; Braeck and Podladchikov, 2007; Thielmann et al., 2015), seismological studies (Prieto et al., 2013), and experiments (Ohuchi et al., 2017) have shown that thermal runaway is possible within the lithospheric mantle and the lower crust (John et al., 2009). Few exhumed pseudotachylyte/mylonite associations have been interpreted to have resulted from ductile instabilities (in the middle to lower crust: Hobbs et al., 1986; White, 1996, 2012; Stewart and Miranda, 2017). Nevertheless, unambiguous microstructural evidence for the process of thermal runaway is missing.

The pseudotachylytes of the Mont Mary nappe (Western Alps; Pennacchioni and Cesare, 1997) are invariably hosted within amphibolite-facies paragneiss ultramylonites. The pseudotachylyte fault veins are sub-parallel to the ultramylonitic foliation, and were formed at the same metamorphic conditions of the ultramylonites. Therefore they represent a candidate for recording thermal runaway. We used electron backscattered diffraction (EBSD) to investigate quartz microstructures and crystallographic preferred orientations (CPO) in the ultramylonite host of pseudotachylytes, and in clasts within pseudotachylytes in order to infer the deformation mechanisms preceding melting. The aim of this study is to understand the rheological evolution of the ultramylonite and to detect signs of localised accelerated creep rate that could eventually have evolved into pseudotachylytes. If thermal runaway was the effective mechanism, we expect the clasts within the pseudotachylytes to show different microstructures and a smaller recrystallised grain size than the host rock, indicative of progressively higher creep rates in the zone that eventually underwent melting. We also expect a gradual decrease in grain size in the host ultramylonite approaching the pseudotachylyte veins (e.g. Thielmann et al., 2015).

2. Geologic setting and sample description

The upper tectonic unit of the Mont Mary nappe (Fig. S1) consists of upper amphibolite- to granulite-facies paragneisses, metabasites and marbles (Canepa et al., 1990). The well-preserved main metamorphic imprint is pre-Alpine (Permian: Manzotti et al., 2014 and references therein), while pervasive Alpine greenschist-facies retrogression is restricted to mylonitic shear zones at the tectonic unit boundary. The Mont Mary nappe represents an allochthonous slice of pre-Alpine lower continental crust, involved in the Alpine orogenesis and inserted in the stack of Alpine nappes. This lower crustal level is preserved, outside the Alpine nappe stack, in the Ivrea Zone of the South Alpine Domain, forming the base of a nearly continuous tilted section of the pre-Alpine crust (e.g. Handy, 1987). During Permo-Mesozoic time, this continental crust was extended and the lower crustal rocks were exhumed along lithospheric extensional detachments. Extension eventually resulted in the development of the thinned continental margin of the Tethys Mesozoic ocean. The mylonitic roots of these detachments are represented by the high-grade mylonites, associated with pseudotachylytes, of the Mont Mary unit (and of the Ivrea Zone: Pittarello et al., 2012) described here. The South Alpine Domain also preserves shallower portions of the extensional detachment systems, e.g. the Pogallo tectonic Line, a greenschist-facies mylonitic zone also characterised by abundant pseudotachylytes (Handy, 1987).

The pre-Alpine coarse-grained paragneisses of the Mont Mary nappe consist of quartz + garnet + sillimanite + biotite + plagioclase + K-feldspar + ilmenite + graphite ± cordierite. These rocks host a few-meters-thick horizon of amphibolite-facies mylonite and ultramylonite. The mylonitic rocks show, compared to the protolith: consumption of K-feldspar, development of muscovite, growth of new garnet and recrystallisation of biotite. The pressure-temperature conditions of mylonitisation were estimated at 545 ± 35 °C and 0.35 ± 0.1 GPa (Pennacchioni and Cesare, 1997).

The pseudotachylytes consist of a crystallised matrix of dominant biotite, quartz, plagioclase, and ilmenite including clasts of mainly sillimanite, quartz, and plagioclase. Garnet clasts are rare and, where present, are locally surrounded by a narrow, dendritic rim of new garnet. A detailed petrological description of the Mont Mary pseudotachylytes is given by Pennacchioni and Cesare (1997) and Papa et al. (2018). Pseudotachylytes occur within the ultramylonites as thin fault veins (commonly a few mm thick), subparallel to the host foliation, and local injection veins (up to a few cm thick; Fig. 1). The fault veins occur either as isolated structures or in subparallel arrays. Interacting fault and injection veins locally define sidewall ripout geometries (Fig. 1; Swanson, 1992). Pennacchioni and Cesare (1997) and Papa et al. (2018) inferred that the pseudotachylytes were coeval with the mylonitic deformation based on: (i) the presence of local ductile shearing of pseudotachylytes showing the same kinematics as the host ultramylonite (Fig. 2F); and (ii) the stability of amphibolite facies minerals (sillimanite and An_{35}-plagioclase clasts) in sheared pseudotachylytes together with the incipient growth of new dendritic garnet rimming garnet clasts. Sheared pseudotachylytes are distinguished from the host ultramylonites by the following features: (i) oblique foliation relative to the ultramylonitic layering (Fig. 2F); (ii) absence of the compositional layering typical of mylonites and ultramylonites; (iii) limited elongation of quartz clasts, which differ from the long, continuous quartz ribbons of ultramylonites; and (iv) paucity of garnet (Papa et al., 2018). Pseudotachylytes are only found within ultramylonites.

The ultramylonites display a sub-centimetric layering with the alternation of quartz ribbons, quartz-feldspar layers, and biotite-rich layers (Fig. 2A-B). Plagioclase, garnet, and sillimanite occur as porphyroclasts within biotite-rich layers. The mylonitic microstructure and mineral assemblage are described in detail in Pennacchioni and Cesare (1997) and Pennacchioni et al. (2001). A distinguishing microstructure of ultramylonite is the alternation, with gradational contacts (Fig. 2D), of thin (a few 10s μm thick) layers of finely recrystallised quartz ribbons and optically dark layers (Fig. 2C) consisting of a fine-grained mixture of quartz and biotite (X_{Mg} 0.52-0.59; Pennacchioni and Cesare, 1997). The evolution of the quartz microstructure and CPO in the ultramylonites and in clasts of ultramylonitic quartz within the pseudotachylytes is the focus of the present study.

3. Methods

3.1 Sample selection and preparation

The EBSD analysis was conducted on different thin sections of the pseudotachylyte-hosting ultramylonite MMS42 (Fig.1) for a total of 9 EBSD maps (Table S2). Sample MMS42 was chosen between the 13 mylonitic samples containing pseudotachylytes. All these samples have been investigated by optical microscopy and SEM-BSE imaging and they show very similar quartz microstructures. The selected sample is particularly appropriate for the study, being essentially free of post-kinematic alteration that would have obliterated or blurred the pristine microstructural and petrographic features (as it is locally the case in other samples, due to the exhumation path). This sample was also selected because it displays both a layer-parallel pseudotachylyte vein slightly overprinted by ductile shearing and injection veins with no overprint. The analyses were performed on quartz aggregates of the ultramylonite and of clasts within the pseudotachylyte vein. The maps presented in figures of main text and supplementary material are representative of a larger dataset and the reported textural information is supported by a robust database. Thin sections of ultramylonite were prepared from rock chips cut parallel to the stretching lineation and perpendicular to the (ultra)mylonitic foliation (XZ plane of finite strain ellipsoid). The thin sections were chemically polished with colloidal silica and carbon coated.

3.2 EBSD data acquisition and processing

Electron backscattered diffraction (EBSD) analyses were carried out on a JEOL 7001 FEG SEM equipped with a NordLys Max EBSD detector (AZtec acquisition software, Oxford Instruments) and on a JEOL 6610 tungsten filament SEM equipped with a NordLys Nano detector at the Electron Microscopy Centre of the University of Plymouth. EBSD patterns were acquired on rectangular grids with step sizes of 0.3, 0.35 and 0.4 μm (Table S2). Working conditions during acquisition of EBSD patterns were 20 kV accelerating voltage, 70° sample tilt, high vacuum, and a working distance between 17 and 23 mm.

Noise reduction was performed using the software CHANNEL5 of HKL Technology, Oxford Instruments, by removing wild spikes (i.e. single pixels surrounded by 8 neighbours with different orientations) and replacing zero-solution points with the orientation of nearest neighbours starting from eight neighbours down to five. The pole figures are plotted as equal area, lower hemisphere projections using one point per grain, and oriented with the general shear zone kinematics reference system (X = stretching lineation; Z = pole to foliation). Misorientation axes have been determined in sample and crystal coordinates for ranges of misorientation angles of 2-10° and 10-45°. The threshold of 10° was chosen to separate subgrain boundaries from grain boundaries, and the upper limit of 45° to avoid the contribution of Dauphiné twins in the misorientation axes distribution of grain boundaries. The misorientation axes distributions are plotted in crystal coordinates as equal area, lower hemisphere projections. Contoured projections have constant contouring parameters (halfwidth = 10°).

To avoid any contribution from Dauphiné twin boundaries (misorientation of 60° around the [c] axis), grains were calculated from EBSD data using the point group 622 and transforming the grain mean orientation back into trigonal point group 321, as in Kilian and Heilbronner (2017), using the

MTEX toolbox by Ralf Hielscher (https://mtex-toolbox.github.io/). Grain size was calculated as diameter of the area equivalent circle. The minimum cut-off area was set to 10 pixels, which means that, depending on the map acquisition step size, only grains of a size > 1.07 μm (0.3 μm step size), >1.25 μm (0.35 μm), and 1.43 μm (0.4 μm) were considered. The number-weighted distribution of the grain size is presented as a histogram using 1 μm bins. For piezometric estimates, according to Cross et al. (2017), the root mean square (RMS) of the recrystallised grain size distribution is used. The population of recrystallised grains is segmented in 2 classes of high- and low-strained grains (respectively $quartz_1$ and $quartz_2$ grains) by calculating a threshold grain orientation spread (GOS) value, following the method of Cross et al. (2017). The arithmetic mean of grain size distribution of $quartz_2$ is considered as the average recrystallised grain size. This method was calibrated by Cross et al. (2017) using experimentally deformed samples of Black Hills Quartzite, where large, non-recrystallised grains, with a high degree of intracrystalline lattice distortion are easily distinguished from small recrystallised grains. In the case of a natural mylonite with a prolonged deformation history, it is not so easy to separate old recrystallised grains from those related to the last recrystallisation event. Nonetheless, we followed the procedure in order to obtain representative and reproducible results, but we are aware of the limitations this method involves. Considering only $quartz_1$ grains, and setting the critical misorientation angle to 2°, we used the same procedure as above to calculate subgrain size.

4. Results

The investigated microstructures include both domains distant from the pseudotachylyte and unaffected by the (coseismic) cataclastic deformation (Fig. 3, 4, 5), and fractured domains close to the pseudotachylyte (Fig. S2; see location of all EBSD maps in Fig. S6). Within pseudotachylytes, we have analysed only angular clasts of recrystallised quartz embedded in a pristine pseudotachylyte matrix unaffected by a solid-state ductile overprint (Fig. 6, S2, S3, S4). These clasts can be distinguished from elongated quartz clasts in foliated pseudotachylytes (Fig. 2F).

4.1 Microstructures and CPO of quartz in the ultramylonite

Monomineralic mm-thick quartz layers range from monocrystalline ribbons to dynamically recrystallised aggregates (Fig. 3, 4, 5). In recrystallised ribbons, the grain size is heterogeneous and varies between 1 and 30 μm (Fig. 4C). Using the method of Cross et al. (2017), the recrystallised grain population was segmented into two classes (Fig. 4A): i) larger grains elongated slightly oblique to the ribbon boundary, with a higher degree of internal distortion (*quartz*$_1$); and (ii) smaller, equant, almost strain-free grains (*quartz*$_2$). *Quartz*$_1$ shows abundant subgrains of a similar size as *quartz*$_2$ grains (Fig. 4D). The average grain size of *quartz*$_2$ is 4-5 μm (Fig. 4C, Table S2). *Quartz*$_2$ has a heterogeneous spatial distribution and preferentially occurs at the ribbon boundary adjacent to the mixed quartz + biotite layers (Fig. 4A, 5A). In the recrystallised quartz ribbons, grains with grain size < 5 μm form on average less than 15% of the cross-sectional area (Fig. S3).

The bulk [c]-axis CPO of recrystallised quartz displays a short girdle centered on the Y axis and nearly orthogonal to the foliation, with either 2 maxima symmetrically developed aside Y (Fig. 5C) or a single asymmetric maximum (Fig. 3B). *Quartz*$_1$ and *quartz*$_2$ show very similar pole figures except for a slight weakening of the CPO for *quartz*$_2$ (Fig. 4B). The misorientation axes distribution in crystal coordinates, for both low angle (subgrain) boundaries (2-10°) and high angle (grain) boundaries (10-45°), shows a strong maximum parallel to the [c]-axis (Fig. 3C). The distribution of uncorrelated misorientation angles shows higher frequencies for angles < 60° with respect to the random distribution, while for correlated misorientation angles the distribution shows higher frequencies for angles of 60° (Dauphinè twins) and < 10° (subgrains) (Fig. 3D).

Aggregates of *quartz*$_2$ at the boundaries of recrystallised ribbons transitional to mixed quartz + biotite layers are commonly spatially associated with sillimanite porphyroclasts (Fig. 3A; Fig. 5A). The CPO of these aggregates is similar to the CPO in the ribbon center, but is significantly weaker (Subset B in Fig. 5C). The misorientation axes distribution also shows a relatively weaker maximum parallel to [c] and an increased dispersion (Subset B in Fig. 5C). The distribution of uncorrelated misorientation angles at the ribbon periphery is close to a random distribution (Subset B in Fig. 5C). *Quartz*$_2$ grains dominate the microstructure at the ribbon boundary: the average grain size is smaller than 3 μm and most grains are smaller than 10 μm (Fig. 5G). The few *quartz*$_1$ grains are smaller than inside the ribbons and contain subgrains of a similar size as *quartz*$_2$ grains (Fig. 5E).

The aggregates of dominant *quartz*$_2$ at the ribbon boundary display common four-grain junctions (Fig. 5E) and aligned, straight grain boundaries. Locally, isolated grains of a second phase, non-indexed in EBSD maps, are present between *quartz*$_2$ grains (Fig. 5E). Towards the mixed quartz + biotite layer, the *quartz*$_2$ aggregate is locally disrupted, along the grain boundaries nearly orthogonal to the ribbon boundary, to form single-grain-thick columns separated by biotite (Fig. 5D). Biotite is preferentially oriented with the basal plane orthogonal to the quartz columns and subparallel to the foliation (Fig. 2E; Fig. 5D). This microstructure is transitional with mixed quartz + biotite layers where small (< 2.5 μm in diameter) strain-free quartz grains occur isolated within the biotite matrix (Fig. 2D; Fig. 2E; Subset C in Fig. 5B). This transition is associated with the progressive weakening of the CPO of the *quartz*$_2$ and eventually results in an almost random CPO and in a random distribution of uncorrelated misorientation angles (Subset C in Fig. 5C). Subgrain and grain boundaries show an increased dispersion of misorientation axes (Subset C in Fig. 5C).

The above described quartz ribbons are mostly unaffected by coseismic cataclastic deformation and are only locally crosscut by fractures discontinuously decorated by a very thin layer of pseudotachylyte and/or ultracataclasite. Adjacent to pseudotachylyte (Fig. S2), coseismic deformation is more pervasive (Fig. S2B) and the quartz ribbons are offset by sharp micro-shear zones that, in EBSD maps, consist of aggregates, a few tens of μm thick, of fine (2-3 μm grain size) strain-free quartz grains. These micro-shear zones show a host-controlled CPO that, in both the analysed cases, is weaker than the CPO in the quartz ribbons. The microstructure of these fine aggregates is very similar to the coseismic ultrafine dynamic recrystallised quartz described in Bestmann et al. (2011) and to quartz microstructures observed in 'kick and cook' experiments by Trepmann et al. (2007). In at least one of these bands we observe a clear maximum of the misorientation axes of subgrain boundaries parallel to the (π') direction, which is not present in the host rock (Fig. S2). Excepting these localised structures, the recrystallised quartz shows a grain size slightly higher (Table S1), and microstructures and misorientation axes distribution identical to the quartz ribbons that are not in close proximity to pseudotachylyte.

4.2 Microstructure and CPO of quartz clasts

The clasts consist of aggregates of recrystallised quartz remarkably similar to the host-rock quartz ribbons (Fig. 6; Fig. S4) in that: (i) the grain size ranges from 1 to > 30 μm, and two grain size classes (internally distorted coarser $quartz_1$ and smaller, strain-free $quartz_2$) can be distinguished (Fig. 6F); (ii) the spatial distribution of $quartz_2$ is heterogeneous, with domains in which $quartz_2$ is scattered within an aggregate of dominant $quartz_1$ and domains in which $quartz_2$ is dominant (respectively the "coarse-grained" and "fine-grained" areas in Fig. 6A); (iii) the elongated $quartz_1$ grains display a shape preferred orientation (Fig. 6A); (iv) $quartz_1$ grains contain subgrains of similar size as $quartz_2$ (Fig. 6F); and (v) four-grain junctions and alignment of straight grain boundaries are common in the aggregates of predominant $quartz_2$ (Fig. 5F; Fig. S5). The main difference with respect to the host ultramylonites is that the quartz aggregates of clasts have a smaller average grain size ($quartz_2$ average grain size: 3-4 μm; Fig. 6F; Fig. S3; Table S1).

The bulk [c]-axis pole figures of quartz within clasts are characterised by an incomplete girdle with either one asymmetric maximum (Fig. 6C; Fig. 6E) or two symmetrical maxima (Fig. S4C) as in the host ultramylonite (though passively rotated during float within the melt). The CPO becomes weaker with decreasing grain size (Fig. 6C). In crystal and sample coordinates the misorientation axes distributions generally have less well developed maxima than in the host ultramylonite. For misorientation angles <10° (subgrain boundaries) a maximum is commonly present between the directions (π’) and (z) and, in just one case, a weak maximum is parallel to [c]. Misorientation axes of grain boundaries show either a nearly random distribution or one weak maximum parallel to [c] (Fig. 6D; Fig. S4B; Fig. S5B). Uncorrelated misorientation angles grade toward the uniform distribution curve moving from coarse-grained to fine-grained areas (M-index diminishes from 0.30 to 0.18), and correlated misorientation angles show maximum values at small angles (< 15°) in addition to the maximum at around 60° (Dauphinè twins) (Fig. 6C; Fig. 6E).

A micrometric film of a second phase is commonly present along grain boundaries (Fig. 6B). This is not associated with further weakening of the CPO and no development of columnar quartz or mixed biotite + quartz layers was observed.

5. Discussion

5.1 Deformation mechanisms of quartz in ultramylonite

In the ultramylonite, monomineralic quartz layers underwent recrystallisation by dominant subgrain rotation resulting in a strong CPO. The short girdle centered on the Y-axis in the [c]-axis pole figures of recrystallised quartz is typical of prism<a> and rhomb<a> intracrystalline slip (e.g. Schmid and Casey, 1986). Subgrain boundary misorientation axes maxima correspond to axes of tilt boundaries of {m}<a>, {r}<a>, and {π}<a> slip systems and to combinations of twist boundaries for {z}<a>, and {π’}<a> (Lloyd et al., 1997). These features have been commonly observed in quartz mylonites deformed at amphibolite facies conditions (e.g. Stipp et al., 2002; Toy et al., 2008). The similarity between subgrain size and recrystallised grain size indicates negligible grain growth after subgrain rotation recrystallisation.

The heterogeneous grain size and the similar CPO for larger and smaller grains suggest that dynamic recrystallisation occurred at non-steady state differential stresses under constant temperature, as there is no evidence of changes in the P-T conditions of deformation during mylonitisation (i.e., no evidence of syn-kinematic retrograde metamorphic reactions of biotite, garnet and sillimanite). The average recrystallised grain size in quartz ribbons is 4-5 μm, but overall the number weighted distribution of grain sizes is largely dominated by grains smaller than 4 μm. The smallest new grains (2.5 μm average grain size) dominate in foliation-parallel bands of nearly complete recrystallisation. The aggregates of fine recrystallised grains are commonly spatially associated with sillimanite grains that acted as stress risers within the ribbon (Fig. 5A; e.g. Cross et al., 2015). This process resulted in a decrease in the recrystallised grain size of quartz which, in turn, promoted a change in deformation mechanism within the aggregate. The weakening of the CPO and of the spatial density of misorientation axes of grain boundaries, the development of four-grain junctions and the alignment of straight grain boundaries all suggest that grain boundary sliding (GBS) became increasingly active within the finest grained aggregates (e.g. White, 1979). The transition from dominant dislocation creep to dominant GBS has been already inferred for quartz in ultrafine recrystallised aggregates (Behrmann and Mainprice, 1986; Kilian et al., 2011; Fukuda et al., 2018). In the Mont Mary ultramylonites, after recrystallisation by subgrain rotation produced an aggregate dominated by small grains, GBS and associated cavitation (Fusseis et al., 2009; Kilian et al., 2011) subsequently promoted opening along the grain boundaries accommodated by biotite precipitation. Cavitation preferentially occurred along grain boundaries aligned orthogonal to the ribbon, as also observed by Kilian et al. (2011). This resulted in the development of the columnar quartz microstructure (Fig. 5D). Syn-kinematic precipitation of biotite along the opening grain boundaries is indicated by the strong preferred orientation of biotite orthogonal to cavitation pore walls (Fig. 2E). This process eventually ended in complete disintegration of the quartz aggregate and a transition to a mixed quartz + biotite matrix. Pinning by a second phase impeded grain growth and caused a permanent switch from dislocation creep to grain size sensitive (GSS) creep. Dynamic recrystallisation of quartz grains, embedded in the softer biotite matrix, was no longer possible and further quartz grain deformation was instead achieved by dissolution-precipitation processes (Kilian et al., 2011).

5.2 Deformation mechanisms of quartz in pseudotachylyte clasts

Quartz clasts within pseudotachylyte veins show microstructures similar to those of the host ultramylonite, with the important distinction that the degree of fine recrystallisation is consistently higher for all the analysed clasts (Fig. S3). This suggests that pseudotachylytes could have developed from more strongly sheared and more pervasively finely recrystallised ultramylonitic layers than those preserved in the host ultramylonite. The clasts in pseudotachylyte do not show the peripheral disintegration into quartz + biotite by the cavitation process observed in the ultramylonites; these would be unlikely to survive melting due to the low melting temperature of biotite. The subgrain boundaries misorientation axes generally show a wide maximum between the (π’) and (z) directions suggestive of an enhanced activity of the rhomb <a> slip system with respect to the host ultramylonite. In one case, a weak maximum parallel to (m), possibly related to activity of basal <a> slip system, was observed. A switch from dominant prism <a> to a combination of prism, rhomb, and basal <a> intracrystalline slip can be interpreted in terms of increase of differential stress (e.g. Tokle et al., 2019), or decrease in temperature (e.g. Stipp et al., 2002), although the concept of temperature dependency of <a> slip systems has been challenged by Kilian and Heilbronner (2017). The common observation of misorientation axes of subgrain boundaries oriented parallel to the (π’) direction in clasts and in a coseismic recrystallisation band in quartz ribbons at the vein boundary (Fig. S2) suggests that the fine recrystallised grains in clasts partly developed during coseismic deformation (Bestmann et al., 2011; Trepmann et al., 2007). This could explain the increased pervasivity of fine recrystallisation in quartz clasts with respect to host-ultramylonite ribbons. However, the different activation of slip systems can also be interpreted in terms of differences in orientation of the original quartz ribbon with respect to the kinematic framework (Ceccato et al., 2017).

5.3 Paleopiezometry and rheological model

Figure 7A displays the deformation mechanism map of quartz calculated for the deformation conditions of the Mont Mary ultramylonites. The flow law of Hirth et al. (2001) is used to calculate the dislocation creep component of the strain rate:

(1) $\dot{\varepsilon} = A f_h \sigma^n e^{(-Q/RT)}$,

where A is the pre-exponential factor (MPa^{-n} s^{-1}); f_h is the water fugacity (MPa); σ is the differential stress (MPa); n is the stress exponent; Q is the activation energy ($J\ mol^{-1}$); R is the gas constant ($J\ K^{-1}\ mol^{-1}$); and T is the temperature (K). The Mont Mary mylonites had previously been considered to develop under water-deficient conditions based on: (i) the occurrence of synkinematic water-consuming reactions; (ii) the high differential stress during mylonitisation; (iii) the association of mylonites and pseudotachylytes at amphibolite facies conditions (Pennacchioni and Cesare, 1997); and (iv) the grain boundary morphology of recrystallised quartz (Mancktelow and Pennacchioni, 2004). Nevertheless, the observed healing by biotite precipitation of cavitation pores in ultramylonites indicates that conditions were not totally dry.

The flow law for thin-film pressure solution by den Brok (1998) was used to calculate the grain size sensitive (GSS) component of creep:

(2) $\dot{\varepsilon} = C \frac{\rho_f}{\rho_s} \frac{\sigma^n}{d^m} \frac{VcD_w}{RT}$,

where C is a shape constant, ρ_f and ρ_s are the fluid and solid densities (kg/m^3), d is the grain size (μm), m is the grain size exponent, V is the molar volume ($\mu m^3/mol$), c is the solubility of the solid in the fluid phase (molar fraction), and D_w is the diffusivity of the solid in the grain-boundary fluid ($\mu m^2\ s^{-1}$).

Differential stress during deformation was estimated using the “sliding resolution” piezometer of Cross et al. (2017). The creep of quartz in ultramylonites is considered to have taken place at the temperature and pressure conditions estimated by Pennacchioni and Cesare (1997) of 545 °C and

0.35 GPa for mylonitisation. All the flow laws parameters and details for derivation of deformation maps are given in the supplementary material.

Figure 7A indicates that the finest-grained aggregates of the host ultramylonite (RMS ≅ 3 μm) developed at a differential stress in excess of 200 MPa and a strain rate of about 10^{-9} s^{-1}. In the deformation mechanism map, these values plot in the field of dislocation creep very close to the boundary to GSS creep (Fig. 7A). The transition from dislocation creep to GBS is recorded by the occurrence of cavitation in the finest grained recrystallised quartz aggregates and by their disintegration, assisted by precipitation of biotite in micro-cavitation spaces. This transition likely resulted in weakening, which could imply either an increase in strain rate if the shear zone evolved at constant stress, or, vice versa, a stress drop at constant strain rate. The application of paleopiezometry here is justified by the observation that the new finest recrystallised grains still developed by subgrain rotation before the grain boundaries started to slide and cavitate.

The largest recrystallised grains in quartz ribbons of the host ultramylonite (~ 30 μm) record differential stresses of about 50 MPa and a strain rate in excess of 10^{-11} s^{-1}, i.e. two orders of magnitude slower. In the two-stage deformation experiments on quartzite at increasing differential stress of Kidder et al. (2016), the resulting recrystallised grain size distribution is bimodal, therefore preserving the record of both the earlier lower stress state and the later high stress one. In the Mont Mary shear zone, where the stress evolution was likely more complex, we can assume that the largest recrystallised grain size records lower differential stress conditions during the mylonitic deformation which subsequently evolved to higher differential stress in ultramylonites. A similar approach was adopted by Campbell and Menegon (2019), who interpreted quartz microstructures within a granulitic pseudotachylyte-bearing shear zone from Lofoten (Norway) as the result of nonsteady-state flow during postseismic relaxation. We also calculated deformation maps using (i) the flow law for fine-grained quartz aggregates deforming by mixed diffusion and dislocation creep by Fukuda et al. (2018), and (ii) the flow law for dislocation creep of quartz deformed at high differential stresses and low temperatures by Tokle et al. (2019). The results are not dissimilar and are shown in the supplementary material (Fig. S9).

In a simplified rheological model of quartzitic crust (Fig. 7B), formation of the Mont Mary ultramylonites along a Permian extensional detachment (Pennacchioni and Cesare, 1997) occurred close to the brittle-ductile transition. Assuming that pressure, temperature, and depth remained the same for the low- and high-stress stages, the change in strain rate produced a ca. 3-km downward shift of the brittle-ductile transition. Considering the high-strain rate flow and assuming a depth of 14 km, the associated differential stress is close to the brittle strength of extensional faults, calculated assuming dry conditions (pore fluid factor $\lambda = 0$) and a friction coefficient of 0.7. In our simplified model, we assumed that the mylonitic foliation was optimally oriented for reactivation as shear fracture.

5.4 Thermal runaway

Ductile instabilities potentially develop from the positive feedback between shear heating and strain rate in a shear zone, a process known as thermal runaway (Kelemen and Hirth, 2007; Braeck and Podladchikov, 2007; John et al., 2009; Thielmann et al., 2015). This process has been suggested to explain the association of coeval pseudotachylytes and mylonites in the deep crust (Hobbs et al., 1986; White, 1996, 2012; Stewart and Miranda, 2017).

Localised zones of finely recrystallised grain size and elevated strain rates may represent ideal precursors for thermal runaway (Thielmann et al., 2015), provided that the differential stress exceeds a critical threshold. Thielmann et al. (2015) showed that pinning due to secondary phases favors the instability by inhibiting grain growth. In the Mont Mary samples, pseudotachylytes are only found within ultramylonites and quartz clasts within pseudotachylytes show a more extensive grain size reduction than in the host ultramylonite. These observations may suggest that pseudotachylytes developed from zones where thermal runaway was favored by strong grain size reduction and high strain rate, although there is no evidence of a decrease in grain size in the host ultramylonite approaching the pseudotachylyte veins.

We use the model presented in Thielmann et al. (2015) and Thielmann (2018) to estimate whether thermal runaway is a viable process to generate pseudotachylytes under the deformation conditions recorded in the Mont Mary ultramylonites. In this model, a viscoelastic slab is deformed in simple shear, taking into account the evolution of both grain size and temperature (see Thielmann, 2018 for a detailed derivation of the model and the solution procedure). Here, we assume a 1 km thick slab deformed in simple shear. In the middle of the slab, we inserted a 2 m wide zone where the rheological parameters are perturbed by increasing the strain rate of both dislocation creep and GSS creep by a factor of 10, thus inducing a rheological contrast between the central zone and the surrounding matrix (additional material parameters, numerical details, and a study of the impact of perturbing both rheological and grain growth parameters can be found in the supplementary material). 527 simulations were performed at different background strain rates (ranging from 10^{-10} to 10^{-6} s^{-1}) and temperatures (ranging from 400 to 700 °C). The peak differential stress and the maximum achieved temperature were recorded for each simulation. Simulations were aborted whenever temperatures exceeded 1427 °C (1700 K), as melting would certainly have occurred at this temperature. Such high temperatures are only reached in these models in simulations exhibiting thermal runaway, which is why we used the maximum temperature as an indicator of thermal runaway. Figure 8 shows the numerical model results. Each simulation is indicated with a circle, with the circle colour indicating the maximum temperature obtained during the simulation. Peak differential stresses are shown in the background in greyscale, with white contour lines denoting certain differential stress levels. The solid red line in Fig. 8 separates the simulations exhibiting thermal runaway from simulations not resulting in instability.

Model results indicate that thermal runaway can be achieved in a quartz-rich crust, provided that rheological contrasts (which were induced in the models by perturbing the rheological prefactors) within the crust are large enough. Critical differential stresses at the regime boundary range from approximately 250 to 500 MPa. In the ranges of temperature and strain rate estimated for the Mont Mary ultramylonites the model predicts a stable behaviour. However, a slightly faster strain rate of approximately $5*10^{-9}$ s^{-1} could trigger thermal runaway at a critical differential stress (~ 250 MPa), which, at the inferred depth of the Mont Mary mylonites (10-18 km) is comparable to the brittle strength of rocks (Fig. 7B).

The microstructural analysis of Mont Mary ultramylonite and of survivor clasts in pseudotachylyte provides evidence that melting was preceded by a local switch in the dominant deformation mechanism of quartz from dislocation creep to GBS. Stewart and Miranda (2017) interpreted similar microstructures in a pseudotachylyte-mylonite association from the South Mountains metamorphic core complex in Arizona as evidence for ductile instabilities. They argued that GBS domains in the mylonitic quartz aggregates record ductile instabilities triggering pseudotachylyte nucleation due to high strain rate/low effective viscosity during GBS creep. We tend to discard this interpretation for the Mont Mary ultramylonites, since the mechanism of GBS is followed by cavitation and precipitation of biotite in pore spaces. Therefore, the strain rate-limiting process during quartz disintegration is the rate of fluid-assisted precipitation of oriented biotite, which cannot occur at seismic rates. Although the switch to GBS induces a weakening that may initiate instability, Thielmann (2018) showed that the weakening associated with dislocation-accommodated GBS is such that critical runaway differential stresses are never reached. Once the mixed layer of biotite and quartz is fully developed, the associated weakening will impede the development of thermal runaway. Therefore, although the model shows that thermal runaway is possible in a quartzitic rock at conditions comparable to those we estimated for our case study, the microstructural record preserved in the highest strain microstructures of the Mont Mary ultramylonites apparently excludes that thermal runaway did actually occur. It is also worth noting that the numerical results presented here represent the best scenario for thermal runaway, i.e., assuming a different rheological perturbation, critical differential stresses could be higher. Critical differential stresses shown in Fig. 8 must therefore be considered as minimum estimates.

5.5 Failure mechanisms

Microstructures in the Mont Mary ultramylonite record a multi-stage process of subgrain rotation recrystallisation where narrow, ultrafine-grained aggregates associated with high differential stresses (>200 MPa), overprinted coarser recrystallised grains representative of lower differential stresses (c.a 50 MPa). Fitz Gerald et al. (2006) described a similar distribution of quartz grain size for a mylonitic pegmatite from the same Mont Mary shear zone, with coarse (100 μm) recrystallised grains partially mantled by equant, polygonal grains a few μm in size. Such an increase in differential stress is not related to any temperature decrease, since the synkinematic amphibolite-facies mineral assemblage is stable in the ultramylonites. There is no evidence of sources for local stress amplification, such as the arrangement of the Mont Mary mylonites in a networks of intersecting shear zones, that could cause strain incompatibilities and block rotation (Hawemann et al., 2019; Campbell et al., 2020). Instead, there is the indication, from the comparison with the Ivrea zone, that the Mont Mary mylonites belonged to a crustal-scale detachment system where shallower and lower temperature segments (e.g. the Pogallo Line), connected to the brittle seismogenic crust, also include greenschist facies mylonites associated with pseudotachylytes. We therefore infer that the observed high strain rate/differential stress evolution in the ultramylonite resulted from transient, externally-induced change of boundary conditions under constant ambient temperature (Campbell and Menegon, 2019).

The strain rate of 10^{-9} s^{-1} estimated for the finest grained quartz of ultramylonites lie at the higher end of the typical range of strain rates for quartz dislocation creep in shear zones (Fagereng and Biggs, 2019). Such accelerated creep rates and high differential stress can be related to major seismic events occurring in the upper crust that altered the steady state conditions of ductile flow in the underlying crustal domains (Ellis and Stöckhert, 2004). The accelerated creep rates could have triggered thermal runaway during ongoing viscous creep in the Mont Mary ultramylonites, but their microstructural record apparently excludes that thermal runaway did occur. Thus, an alternative failure mechanism must be invoked for the generation of the Mont Mary pseudotachylytes.

Figure 7B shows that the differential stresses recorded in the finest-grained portions of the host ultramylonite are close to the brittle failure criterion for an extensional fault. This suggests that pseudotachylytes may develop within the ductile portion of the crust due to the strain-rate dependent, transient deepening of the brittle-ductile transition following a major earthquake in the seismogenic upper crust. This process may enable brittle failure at temperatures at which a quartz-rich rock should be able to flow at much lower differential stresses if the strain rate is within a typical range for mylonitic shear zones. According to this interpretation, the Mont Mary pseudotachylytes may represent aftershock seismicity related to major events in the upper crust (Jamtveit et al., 2018; Cheng and Ben-Zion, 2019).

6. Conclusions

Numerical modelling shows that thermal runaway could be a viable mechanism for earthquake nucleation in the middle to lower crust for a quartz rheology. The conditions we determined for the Mont Mary ultramylonites are not far from the switch between stable flow and thermal runaway as predicted from the model. However, the entire microstructural evolution of quartz recorded in ultramylonites is compatible with aseismic flow. The observed overprinting of a high differential stress (> 200 MPa) deformation phase over a lower differential stress microstructure under roughly constant temperature might be explained by transients of accelerated creep induced in the ductile crust by stress transfer from a seismogenic source in the upper crust (Ellis and Stöckhert, 2004; Jamtveit et al. 2018; Cheng and Ben-Zion, 2019). Transients of high strain rate in the lower crust can lead to brittle failure if the strain rate is high enough to cause a rheological switch due to the transient downward migration of the brittle-ductile transition. Our calculations show that this could have occurred for the Mont Mary ultramylonites.

Acknowledgements

The staff at University of Plymouth Electron Microscopy Centre is thanked for assistance during EBSD data acquisition. We acknowledge financial support from the University of Padova (BIRD175145/17: "The geological record of deep earthquakes: the association pseudotachylyte-mylonite" awarded to GP), from the Foundation "Ing. Aldo Gini" (scholarship for a long stay abroad awarded to SP), and from the UK Natural Environmental Research Council (grant NE/P001548/1 "The Geological Record of the Earthquake Cycle in the Lower Crust" awarded to LM). Alberto Ceccato is thanked for help with rheological calculations and with Channel5. Luiz Grafulha Morales and Giovanni Toffol are thanked for help with MTEX. We acknowledge three anonymous reviewers for their constructive comments that greatly improved the manuscript and Lucy Campbell for her friendly review of the manuscript.

Appendix A. Supplementary data

References

Behrmann, J. H., and Mainprice, D., 1987, Deformation mechanisms in a high-temperature quartz-feldspar mylonite: evidence for superplastic flow in the lower continental crust: Tectonophysics, v. 140(2-4), p. 297-305, https://doi.org/10.1016/0040-1951(87)90236-8.

Bestmann, M., Pennacchioni, G., Frank, G., Göken, M., and De Wall, H., 2011, Pseudotachylyte in muscovite-bearing quartzite: Coseismic friction-induced melting and plastic deformation of quartz: Journal of Structural Geology, v. 33(2), p. 169-186, https://doi.org/10.1016/j.jsg.2010.10.009.

Braeck, S., and Podladchikov, Y. Y., 2007, Spontaneous thermal runaway as an ultimate failure mechanism of materials: Physical Review Letters, v. 98, p. 095504(1-4), DOI: 10.1103/PhysRevLett.98.095504.

Campbell, L. R., and Menegon, L. (2019). Transient High Strain Rate During Localized Viscous Creep in the Dry Lower Continental Crust (Lofoten, Norway). Journal of Geophysical Research: Solid Earth, v. 124(10), p. 10240-10260. https://doi.org/10.1029/2019jb018052.

Campbell, L. R., Menegon, L., Fagereng, Å., and Pennacchioni, G., 2020, Earthquake nucleation in the lower crust by local stress amplification: Nature Communications, v. 11(1), p. 1-9, https://doi.org/10.1038/s41467-020-15150-x.

Canepa, M., Castelletto, M., Cesare, B., Martin, S., and Zaggia, L., 1990, The Austroalpine Mont Mary Nappe (Italian Western Alps): Memorie di Scienze Geologiche, v. 42, p. 1-17.

Ceccato, A., Pennacchioni, G., Menegon, L., and Bestmann, M., 2017, Crystallographic control and texture inheritance during mylonitization of coarse grained quartz veins: Lithos, v. 290, p. 210-227, DOI: 10.1016/j.lithos.2017.08.005.

Cheng, Y., and Ben-Zion, Y., 2019, Transient Brittle-Ductile Transition Depth Induced by Moderate-Large Earthquakes in Southern and Baja California: Geophysical Research Letters, v. 46(20), p. 11109-11117, https://doi.org/10.1029/2019GL084315

Cross, A. J., Prior, D. J., Stipp, M., and Kidder, S., 2017, The recrystallized grain size piezometer for quartz: An EBSD-based calibration. Geophysical Research Letters, v. 44(13), p. 6667-6674, doi:10.1002/2017GL073836.

Cross, A. J., Kidder, S., and Prior, D. J., 2015, Using microstructures and TitaniQ thermobarometry of quartz sheared around garnet porphyroclasts to evaluate microstructural evolution and constrain an Alpine Fault Zone geotherm: Journal of Structural Geology, v. 75, p. 17-31, http://dx.doi.org/10.1016/j.jsg.2015.02.012.

Den Brok, S. W. J., 1998, Effect of microcracking on pressure-solution strain rate: The Gratz grain-boundary model: Geology, v. 26(10), p. 915-918, https://doi.org/10.1130/0091-7613(1998)026<0915:EOMOPS>2.3.CO;2.

Ellis, S., and Stöckhert, B., 2004, Elevated stresses and creep rates beneath the brittle-ductile transition caused by seismic faulting in the upper crust: Journal of Geophysical Research: Solid Earth, v. 109(B5), B05407, doi:10.1029/2003JB002744.

Fagereng, Å., and Biggs, J., 2019, New perspectives on 'geological strain rates' calculated from both naturally deformed and actively deforming rocks: Journal of Structural Geology, v. 125, p. 100-110, https://doi.org/10.1016/j.jsg.2018.10.004.

Fitz Gerald, J. D. F., Mancktelow, N. S., Pennacchioni, G., and Kunze, K., 2006, Ultrafine-grained quartz mylonites from high-grade shear zones: Evidence for strong dry middle to lower crust: Geology, v. *34*(5), p. 369-372, https://doi.org/10.1130/G22099.1.

Fusseis, F., Regenauer-Lieb, K., Liu, J., Hough, R. M., and De Carlo, F., 2009, Creep cavitation can establish a dynamic granular fluid pump in ductile shear zones: Nature, v. 459(7249), p. 974. 10.1038/nature08051.

Fukuda, J. I., Holyoke III, C. W., and Kronenberg, A. K., 2018, Deformation of fine-grained quartz aggregates by mixed diffusion and dislocation creep: Journal of Geophysical Research: Solid Earth, v. 123(6), p. 4676-4696, 10.1029/2017JB015133.

Handy, M.,1987, The structure, age and kinematics of the Pogallo Fault Zone; Southern Alps, northwestern Italy: Eclogae Geologicae Helveticae, v. 80, p. 593-632.

Hawemann, F., Mancktelow, N. S., Pennacchioni, G., Wex, S., and Camacho, A., 2019, Weak and slow, strong and fast: How shear zones evolve in a dry continental crust (Musgrave Ranges, Central Australia): Journal of Geophysical Research: Solid Earth, v. 124(1), p. 219-240, https://doi.org/10.1029/2018JB016559.

Hirth, G., Teyssier, C., and Dunlap, J. W., 2001, An evaluation of quartzite flow laws based on comparisons between experimentally and naturally deformed rocks: International Journal of Earth Sciences, v. 90(1), p. 77-87, https://doi.org/10.1007/s005310000152.

Hobbs, B. E., Ord, A., and Teyssier, C., 1986, Earthquakes in the ductile regime?: Pure and Applied Geophysics, v. 124(1-2), p. 309-336, https://doi.org/10.1007/BF00875730.

Jamtveit, B., Ben-Zion, Y., Renard, F., and Austrheim, H., 2018, Earthquake-induced transformation of the lower crust: Nature, v. 556(7702), p. 487, 10.1038/s41586-018-0045-y.

John, T., Medvedev, S., Rüpke, L. H., Andersen, T. B., Podladchikov, Y. Y., and Austrheim, H., 2009, Generation of intermediate-depth earthquakes by self-localizing thermal runaway: Nature Geoscience, v. 2(2), p. 137-140, DOI: 10.1038/NGEO419.

Kelemen, P. B., and Hirth, G. A., 2007, Periodic shear-heating mechanism for intermediate-depth earthquakes in the mantle: Nature, v. 446, p. 787–790. DOI: 10.1038/nature05717.

Kidder, S., Hirth, G., Avouac, J. P., and Behr, W., 2016, The influence of stress history on the grain size and microstructure of experimentally deformed quartzite: Journal of Structural Geology, v. *83,* p. 194-206, https://doi.org/10.1016/j.jsg.2015.12.004.

Kilian, R., and Heilbronner, R., 2017, Analysis of crystallographic preferred orientations of experimentally deformed Black Hills Quartzite: Solid Earth, v. 8, p. 1095-1117, https://doi.org/10.5194/se-8-1095-2017.

Kilian, R., Heilbronner, R., and Stünitz, H., 2011, Quartz grain size reduction in a granitoid rock and the transition from dislocation to diffusion creep: Journal of Structural Geology, v. 33(8), p. 1265-1284, DOI: 10.1016/j.jsg.2011.05.004.

Lloyd, G. E., Farmer, A. B., and Mainprice, D., 1997, Misorientation analysis and the formation and orientation of subgrain and grain boundaries: Tectonophysics, v. 279(1-4), p. 55-78, https://doi.org/10.1016/S0040-1951(97)00115-7.

Mancktelow, N. S., and Pennacchioni, G., 2004, The influence of grain boundary fluids on the microstructure of quartz-feldspar mylonites: Journal of Structural Geology, v. 26(1), p. 47-69, 10.1016/s0191-8141(03)00081-6.

Manzotti, P., Ballevre, M., Zucali, M., Robyr, M., and Engi, M., 2014, The tectonometamorphic evolution of the Sesia–Dent Blanche nappes (internal Western Alps): review and synthesis: Swiss Journal of Geosciences, v. 107(2-3), p. 309-336, DOI: 10.1007/s00015-014-0172-x.

Ohuchi, T., Lei, X., Ohfuji, H., Higo, Y., Tange, Y., Sakai, T., Fujino, K., and Irifune, T., 2017, Intermediate-depth earthquakes linked to localized heating in dunite and harzburgite: Nature Geoscience, v. 10, p. 771-776, https://doi.org/10.1038/ngeo3011.

Papa, S., Pennacchioni, G., Angel, R.J., and Faccenda, M., 2018, The fate of garnet during (deep-seated) co-seismic frictional heating: the role of thermal shock: Geology, v. 46(5), p. 471-474, https://doi.org/10.1130/G40077.1.

Pennacchioni, G., and Cesare, B., 1997, Ductile-brittle transition in pre-Alpine amphibolite-facies mylonites during evolution from water-present to water-deficient conditions (Mont Mary nappe, Italian Western Alps): Journal of metamorphic Geology, v. 15(6), p. 777-791, https://doi.org/10.1111/j.1525-1314.1997.00055.x.

Pennacchioni, G., Di Toro, G., and Mancktelow, N. S., 2001, Strain-insensitive preferred orientation of porphyroclasts in Mont Mary mylonites: Journal of Structural Geology, v. 23(8), p. 1281-1298, https://doi.org/10.1016/S0191-8141(00)00189-9.

Pittarello, L., Pennacchioni, G., and Di Toro, G., 2012, Amphibolite-facies pseudotachylytes in Premosello metagabbros and felsic mylonites (Ivrea Zone, Italy): Tectonophysics, v. 580, p. 43-57, https://doi.org/10.1016/j.tecto.2012.08.001.

Prieto, G. A., Florez, M., Barrett, S. A., Beroza, G. C., Pedraza, P., Faustino Blanco, J., Poveda, E., 2013, Seismic evidence for thermal runaway during intermediate-depth earthquake rupture: Geophysical Research Letters, v. 40(23), p. 6064–6068, doi:10.1002/2013GL058109.

Scambelluri, M., Pennacchioni, G., Gilio, M., Bestmann, M., Plümper, O., and Nestola, F., 2017, Fossil intermediate-depth earthquakes in subducting slabs linked to differential stress release: Nature Geoscience, v. 10, p. 960-966, https://doi.org/10.1038/s41561-017-0010-7.

Schmid, S. M., and Casey, M., 1986, Complete fabric analysis of some commonly observed quartz c-axis patterns. In: Hobbs, B. E., Heard, H. C., (Eds.), Mineral and rock deformation: Laboratory studies. American Geophysical Union, Geophysical Monograph, v. 36, p. 263-286, 10.1029/GM036p0263.

Sibson, R. H., 1980, Transient discontinuities in ductile shear zones: Journal of Structural Geology, v. 2(1-2), p. 165-171, https://doi.org/10.1016/0191-8141(80)90047-4.

Stewart, C. A., and Miranda, E. A., 2017, The Rheological Evolution of Brittle-Ductile Transition Rocks During the Earthquake Cycle: Evidence for a Ductile Precursor to Pseudotachylyte in an Extensional Fault System, South Mountains, Arizona: Journal of Geophysical Research: Solid Earth, v. 122(12), p. 10643-10665, https://doi.org/10.1002/2017JB014680.

Stipp, M., Stünitz, H., Heilbronner, R., and Schmid, S. M., 2002, The eastern Tonale fault zone: a ‘natural laboratory’ for crystal plastic deformation of quartz over a temperature range from 250 to 700 °C: Journal of Structural Geology, v. 24(12), p. 1861-1884, DOI: 10.1016/S0191-8141(02)00035-4.

Swanson, M. T., 1992, Fault structure, wear mechanisms and rupture processes in pseudotachylyte generation: Tectonophysics, v. 204(3-4), p. 223-242, https://doi.org/10.1016/0040-1951(92)90309-T.

Thielmann, M., Rozel, A., Kaus, B. J. P., and Ricard, Y., 2015, Intermediate-depth earthquake generation and shear zone formation caused by grain size reduction and shear heating: Geology, v. 43(9), p. 791-794, https://doi.org/10.1130/g36864.1.

Thielmann, M., 2018, Grain size assisted thermal runaway as a nucleation mechanism for continental mantle earthquakes: Impact of complex rheologies: Tectonophysics, v. 746, p. 611-623, https://doi.org/10.1016/j.tecto.2017.08.038.

Tokle, L., Hirth, G., and Behr, W. M., 2019, Flow laws and fabric transitions in wet quartzite: Earth and Planetary Science Letters, v. 505, p. 152-161, 10.1016/j.epsl.2018.10.017.

Toy, V. G., Prior, D. J., and Norris, R. J., 2008, Quartz fabrics in the Alpine Fault mylonites: Influence of pre-existing preferred orientations on fabric development during progressive uplift: Journal of Structural Geology, v. 30(5), p. 602-621, doi:10.1016/j.jsg.2008.01.001.

Trepmann, C. A., Stöckhert, B., Dorner, D., Moghadam, R. H., Küster, M., and Röller, K., 2007, Simulating coseismic deformation of quartz in the middle crust and fabric evolution during postseismic stress relaxation—an experimental study: Tectonophysics, v. 442(1-4), p. 83-104, 10.1016/j.tecto.2007.05.005.

Tse, S. T., and Rice J. R., 1986, Crustal earthquake instability in relation to the depth variation of frictional slip properties: Journal of Geophysical Research: Solid Earth, v. 91(B9), p. 9452-9472, https://doi.org/10.1029/JB091iB09p09452.

White, J. C., 1996, Transient discontinuities revisited: pseudotachylyte, plastic instability and the influence of low pore fluid pressure on deformation processes in the mid-crust: Journal of Structural Geology, v. 18(12), p. 1471-1486, https://doi.org/10.1016/S0191-8141(96)00059-4.

White, J. C., 2012, Paradoxical pseudotachylyte–Fault melt outside the seismogenic zone: Journal of Structural Geology, v.38, p. 11-20, https://doi.org/10.1016/j.jsg.2011.11.016.

White, S., 1979, Grain and sub-grain size variations across a mylonite zone: Contributions to Mineralogy and Petrology, v. 70(2), p. 193-202, https://doi.org/10.1007/BF00374448.

FIGURE CAPTIONS

Figure 1

Polished slab of a loose block of pseudotachylyte-hosting amphibolitic ultramylonite (sample MMS42; coordinates 45.805N, 7.410E). The main pseudotachylyte fault vein, indicated by the black arrow, is parallel to the mylonitic foliation and located at the boundary of a quartz-rich layer in the host mylonite. The white arrows indicate melt-bearing contractional ramps part of a 'sidewall ripout' structure, typically associated with pseudotachylytes (Swanson, 1992). In the sketch on the left, the melt is represented in red and quartz-feldspar-rich layers in turquoise.

Figure 2

A) Plane-polarised light image of an array of pseudotachylyte fault vein and injection veins. The pseudotachylyte main vein, parallel to the foliation, was overprinted by ductile shear as shown by an oblique, dextral foliation. Injection veins, intruding at a high angle the host-rock foliation, do not show any ductile overprinting (enlargement of the area enclosed by the black rectangle in 2F). Note the alternation in the host mylonite of quartz-feldspar-rich layers and darker biotite-rich layers. In the upper part of the image, the microstructure is characterised by pervasive cataclastic deformation, mainly represented by shear fractures subparallel to the main injection vein. B) Sketch showing the most relevant features in (A). The white dashed line outlines the boundary between the sheared main pseudotachylyte vein and the unsheared injection vein. Black dashed lines outline the oblique foliation in the sheared pseudotachylyte. C) Detail of a quartz-rich layer, showing an alternation between quartz ribbons and turbid, brownish layers not resolvable with optical microscopy. Note the abundance of small, prismatic porphyroclasts of sillimanite (indicated by black arrows). Plane-polarised light. D) SEM-backscattered image of the same kind of microstructure shown in (C). Turbid layers consist of quartz grains (dark grey) in a matrix mainly composed of biotite (light grey) and small acicular ilmenite crystals (white). E) Detail of a quartz +

biotite layer showing the typical microstructure of columnar, few-microns-thick quartz (black) aggregates, separated by thin vertical biotite (light grey) layers in which biotite lamellae grew with their long axes parallel to the foliation (BSE-image). The foliation (quartz ribbons elongation) is outlined by the white dashed line and is roughly parallel to that of Fig. 2D. White arrows indicate a few locations where biotite crystals growing parallel to the foliation is particularly evident. F) Detail of the pseudotachylyte vein of Fig. 2A, clearly showing dextral oblique foliation and quartz clast elongation.

Figure 3

EBSD analysis of quartz ribbons of the host mylonite. The trace of the mylonitic foliation is horizontal. A) Inverse pole figure map, colour coded with respect to the Y direction, of the selected subset consisting of almost completely recrystallised, non-disintegrated quartz ribbons. Background band contrast image shows layers of partially disintegrated quartz and biotite (black), locally containing sillimanite clasts (coloured in green). B) Contoured pole figure for the (c)-axis. C) Misorientation axis distribution in crystal coordinates for subgrains (2-10°) and grain boundaries (10-45°). Max and min are expressed as multiples of the uniform distribution (m.u.d.). D) Misorientation angle distributions for correlated and uncorrelated misorientations. The red line represents the theoretical random distribution for the point group 321.

Figure 4

A) GOS-separated recrystallised and relict grains for the map shown in Fig. 3A. Border grains have been removed and grains have been calculated considering a hexagonal symmetry to discard twin boundaries. B) (c)-axis contoured pole figure for recrystallised (quartz$_2$) and relict grains (quartz$_1$). Max and min expressed as multiples of the uniform distribution (m.u.d.). C) Grain size distribution for quartz$_2$ and quartz$_1$ grains. D) Grain size distribution for recrystallised grains (quartz$_2$) and subgrains.

Figure 5

EBSD analysis of quartz ribbons of the host mylonite. The trace of the mylonitic foliation is horizontal. A) EBSD maps of quartz grains colour coded according to grain size (diameter of the equivalent circle). Notice that, in non-disintegrated recrystallised quartz ribbons, small (blue and green) grains are preferentially located at the ribbons boundary and especially around the large sillimanite crystal in the right hand side of the map. B) Subsets of (A) analysed in (C). Subset A (red) consists of recrystallised, non-disintegrated quartz ribbons; subset C (blue) consists of quartz grains or aggregates of grains completely detached from the host ribbons and embedded in the biotite matrix. Subset B (green) is transitional between the two. C) (c)-axis contoured pole figures, misorientation axes distribution, and misorientation angle distribution for the subsets in (B). D) Selected area of (A) showing an incipient mixed layer of quartz and biotite between two quartz ribbons. Opening and precipitation of new biotite preferentially along planes perpendicular to the ribbon elongation forms the typical columnar quartz aggregates described in the text. E) Detail of a fine-recrystallised area at ribbon boundary, showing quadruple junctions (white circles) and interstitial biotite grains (not indexed in EBSD maps) at grains junctions (white arrows). Location of this area is indicated in (A). F) Detail of a completely recrystallised area in a quartz clast within pseudotachylyte (see figure S3). Four-grain junctions are common and associated with straight aligned grain boundaries (white circles and red arrows). $Quartz_2$ grains are small and devoid of subgrains. Locally tiny biotite (non-indexed points) is found at four-grain junctions (white arrows). (D), (E), and (F) are inverse pole figures maps colour coded with respect to the Y direction. Boundaries are colour coded like in Fig. 3A. G) Grain size distribution for subset B.

Figure 6

EBSD analysis of quartz clast within pseudotachylyte. A) EBSD map colour coded by grain size (diametre of the equivalent circle). Thick black line separates two subsets in which the microstructure is dominated by fine-grained quartz$_2$ grains (above the line) and coarse-grained quartz$_1$ grains (below the line). B) Backscattered SEM image of the quartz clast. White arrows indicates small iron sulfide droplets. C) (c)-axis contoured pole figures and misorientation angle distributions for the fine-grained area above the thick black line in (A). D) Misorientation axes distribution in crystal coordinates for subgrains (2-10°) and grain boundaries (10-45°) for the whole clast. E) (c)-axis contoured pole figures and misorientation angle distributions for the fine-grained area above the thick black line in (A). F) Grain size distribution for recrystallised (quartz$_2$), relict grains (quartz$_1$), and subgrains for the entire clast.

Figure 7

A) Deformation mechanisms map for quartz with contoured strain rate curves. The red line is the "sliding resolution" piezometer by Cross et al. (2017) while the black dotted line represents the boundary between fields of dominant grain size sensitive and grain size insensitive creep. The two stars correspond to the grain size of coarse recrystallised quartz grains in ribbons (30 μm) and ultrafine aggregates of quartz$_2$ at ribbons boundary (3 μm). Details on the derivation of this map can be found in section 5.3 of the main text and in the supplementary material. B) Simplified crustal strength diagram for quartz, plotted for the strain rates calculated in (A). The frictional sliding law for an extensional fault is used with a friction coefficient of 0.7. The geothermal gradient is 37.4 K/km.

Figure 8

Results of a 1D model coupling the evolution of differential stress, grain size and temperature in a viscoelastic medium for quartz rheology. Each circle indicates a simulation, with colours denoting the maximum temperature reached in the respective simulation (simulations were aborted when temperatures reached values of 1700 K). Peak differential stresses are shown in the background in greyscale, with white contour lines denoting selected differential stress levels. The hand-drawn solid red line separates the thermal runaway regime from the stable regime. The red shaded area approximates the estimated temperature/strain rate conditions for the Mont Mary ultramylonites.

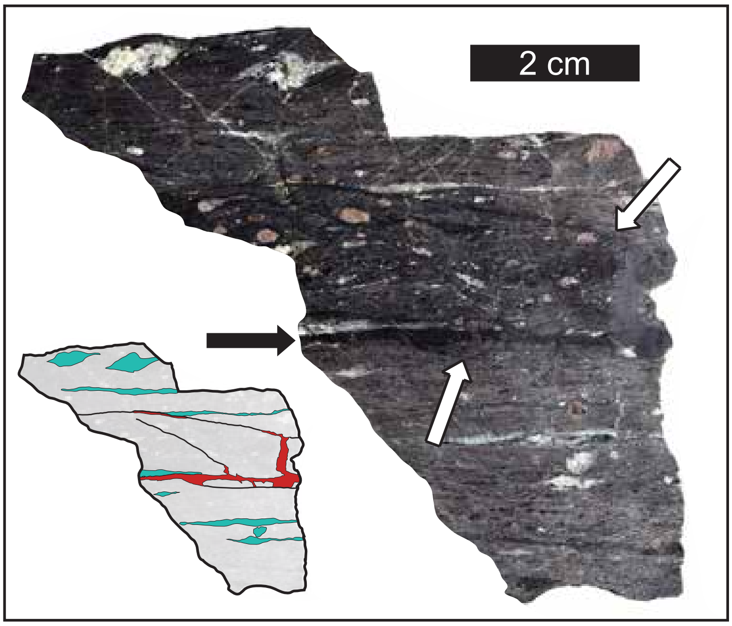
2 cm

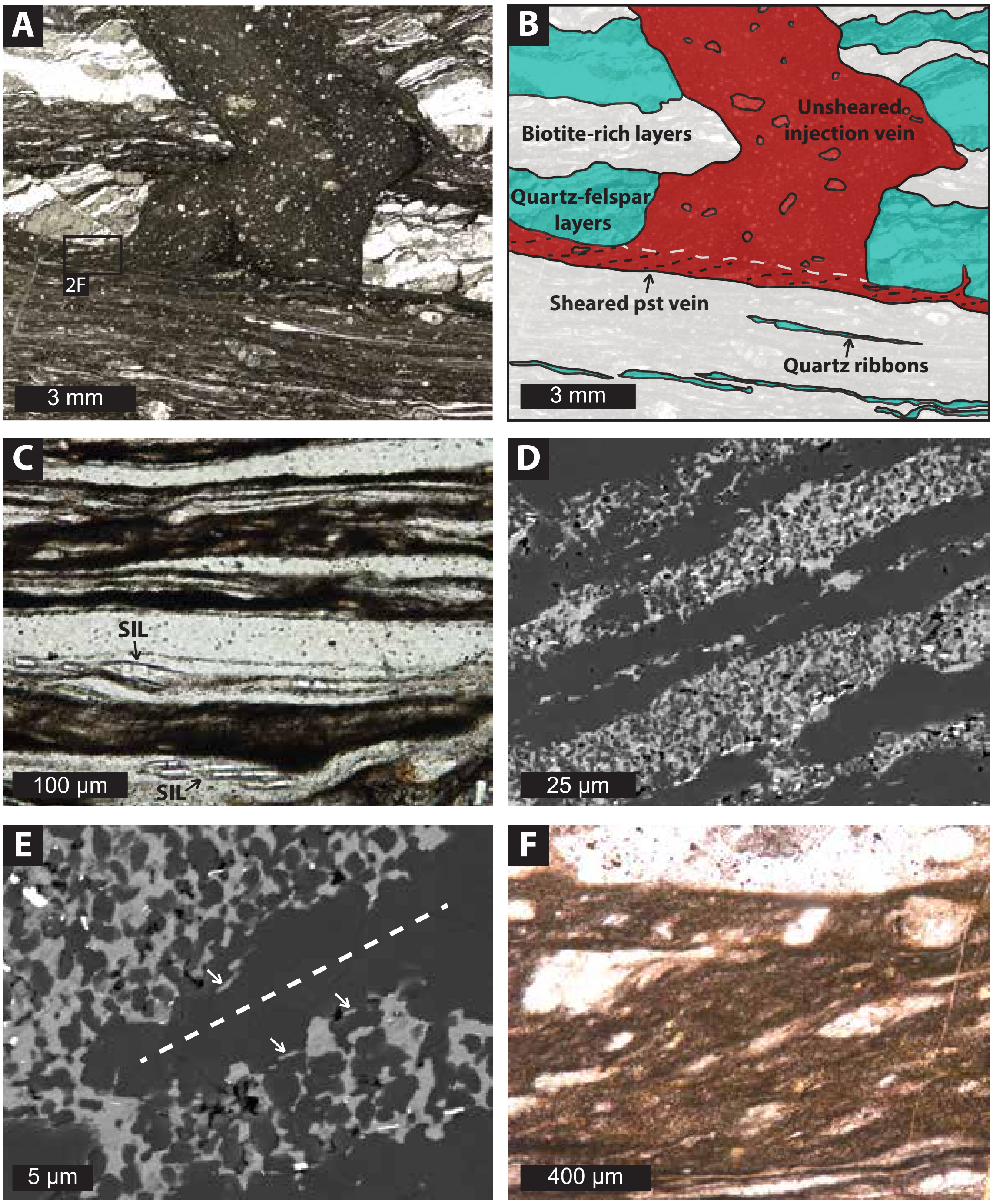
A
2F
3 mm
B
Biotite-rich layers
Unsheared injection vein
Quartz-felspar layers
Sheared pst vein
Quartz ribbons
3 mm
C
SIL
SIL
100 μm
D
25 μm
E
5 μm
F
400 μm

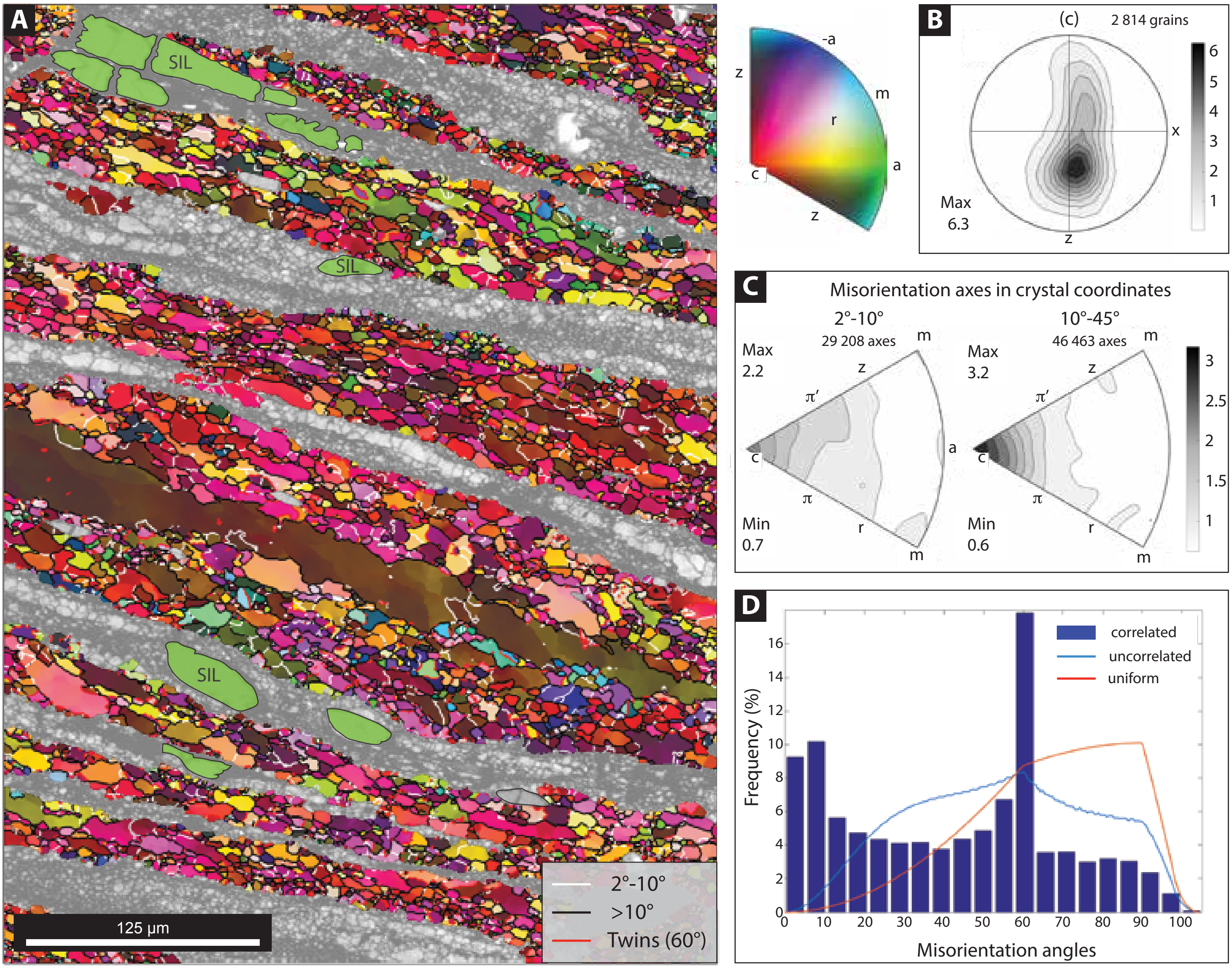

A
SIL
SIL
SIL
125 µm
2°-10°
>10°
Twins (60°)
-a
z
m
r
a
c
z
B
(c)
2 814 grains
x
z
Max
6.3
6
5
4
3
2
1
C
Misorientation axes in crystal coordinates
2°-10°
29 208 axes
Max
2.2
Min
0.7
10°-45°
46 463 axes
Max
3.2
Min
0.6
m
z
π'
c
a
π
r
m
3
2.5
2
1.5
1
D
correlated
uncorrelated
uniform
Frequency (%)
Misorientation angles
0
10
20
30
40
50
60
70
80
90
100
2
4
6
8
10
12
14
16

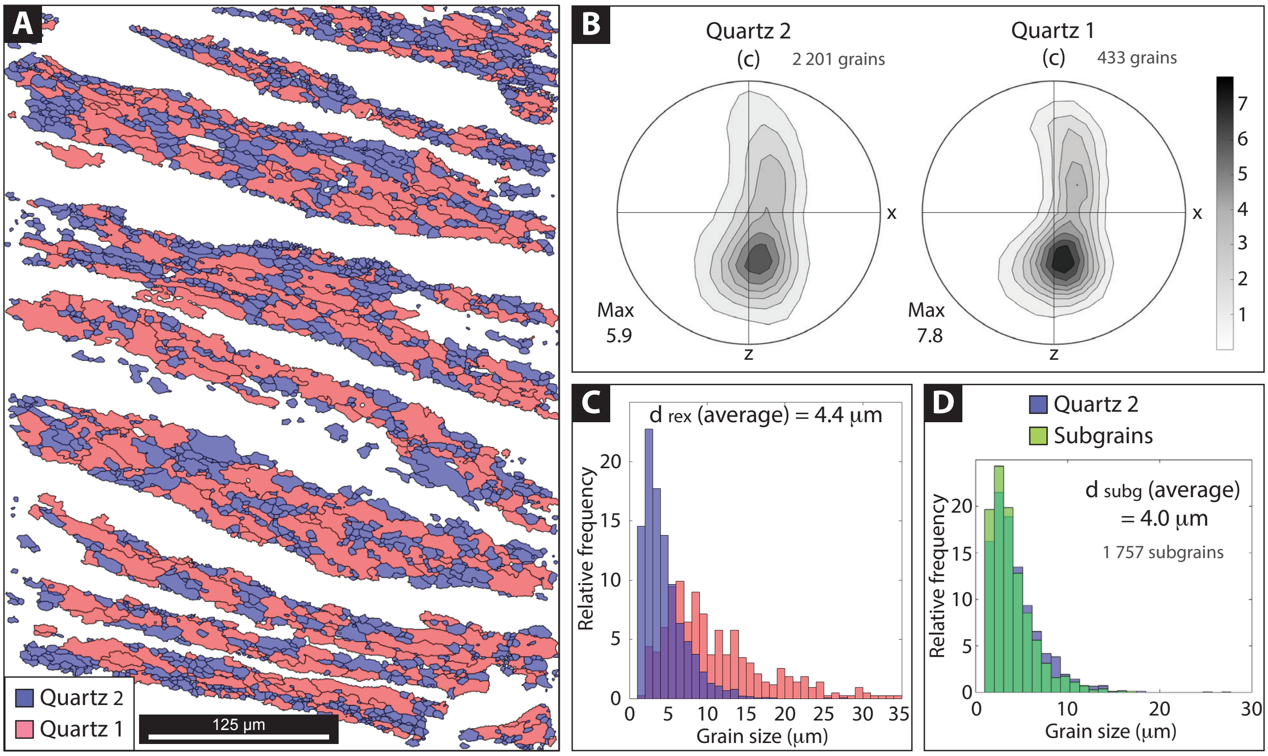

A
Quartz 2
Quartz 1
125 µm
B
Quartz 2
(c)
2 201 grains
Max
5.9
Quartz 1
(c)
433 grains
Max
7.8
x
z
7
6
5
4
3
2
1
C
d rex (average) = 4.4 µm
Relative frequency
Grain size (µm)
0
5
10
15
20
25
30
35
D
Quartz 2
Subgrains
d subg (average)
= 4.0 µm
1 757 subgrains
Relative frequency
Grain size (µm)
0
10
20
30

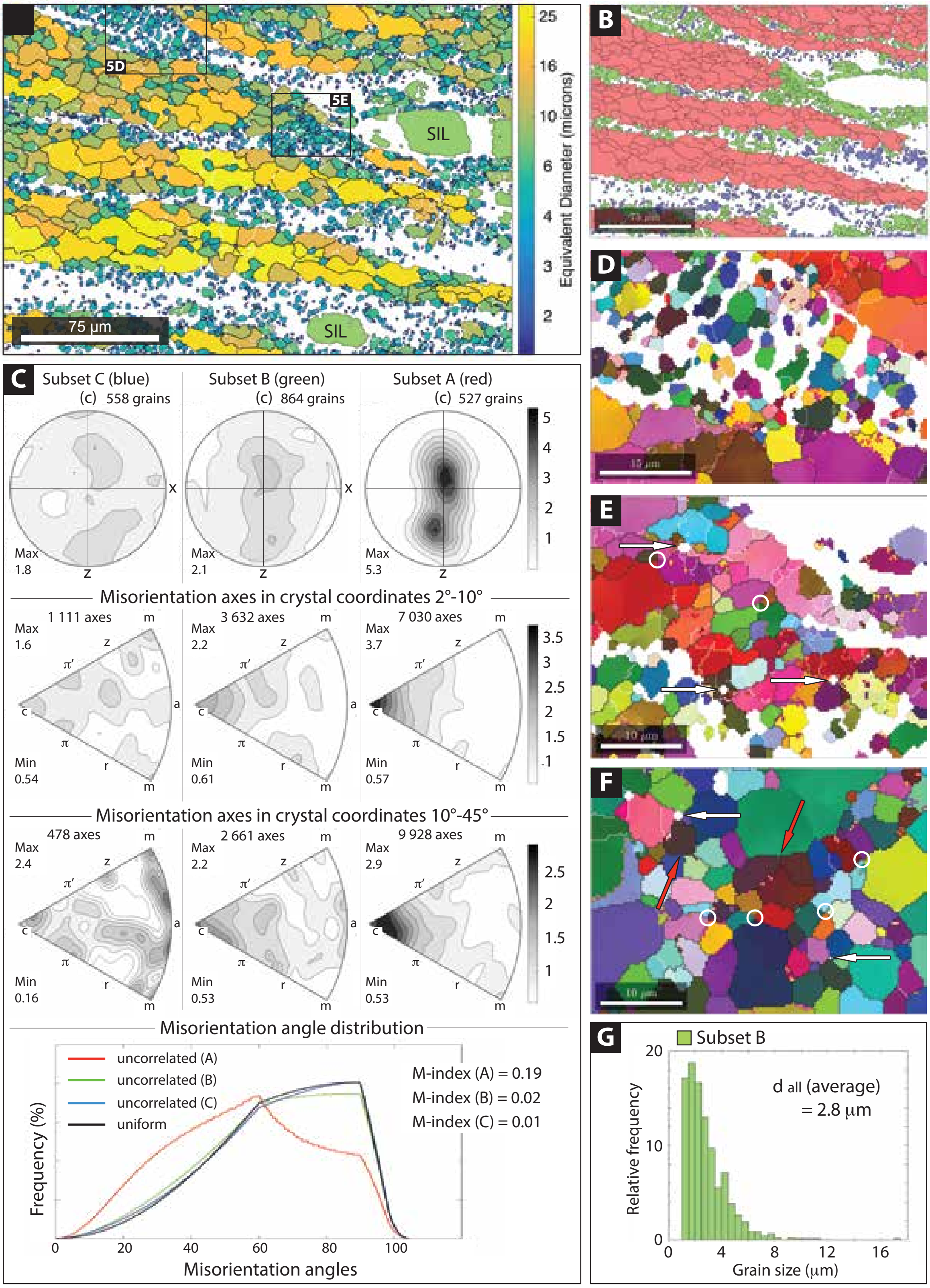
5D
5E
SIL
SIL
75 µm
Equivalent Diameter (microns)
25
16
10
6
4
3
2
B
C
Subset C (blue)
(c) 558 grains
Subset B (green)
(c) 864 grains
Subset A (red)
(c) 527 grains
Max 1.8
Max 2.1
Max 5.3
Misorientation axes in crystal coordinates 2°-10°
1 111 axes
3 632 axes
7 030 axes
Max 1.6
Max 2.2
Max 3.7
Min 0.54
Min 0.61
Min 0.57
Misorientation axes in crystal coordinates 10°-45°
478 axes
2 661 axes
9 928 axes
Max 2.4
Max 2.2
Max 2.9
Min 0.16
Min 0.53
Min 0.53
Misorientation angle distribution
uncorrelated (A)
uncorrelated (B)
uncorrelated (C)
uniform
M-index (A) = 0.19
M-index (B) = 0.02
M-index (C) = 0.01
Frequency (%)
Misorientation angles
D
E
F
G
Subset B
d all (average) = 2.8 µm
Relative frequency
Grain size (µm)

Figure

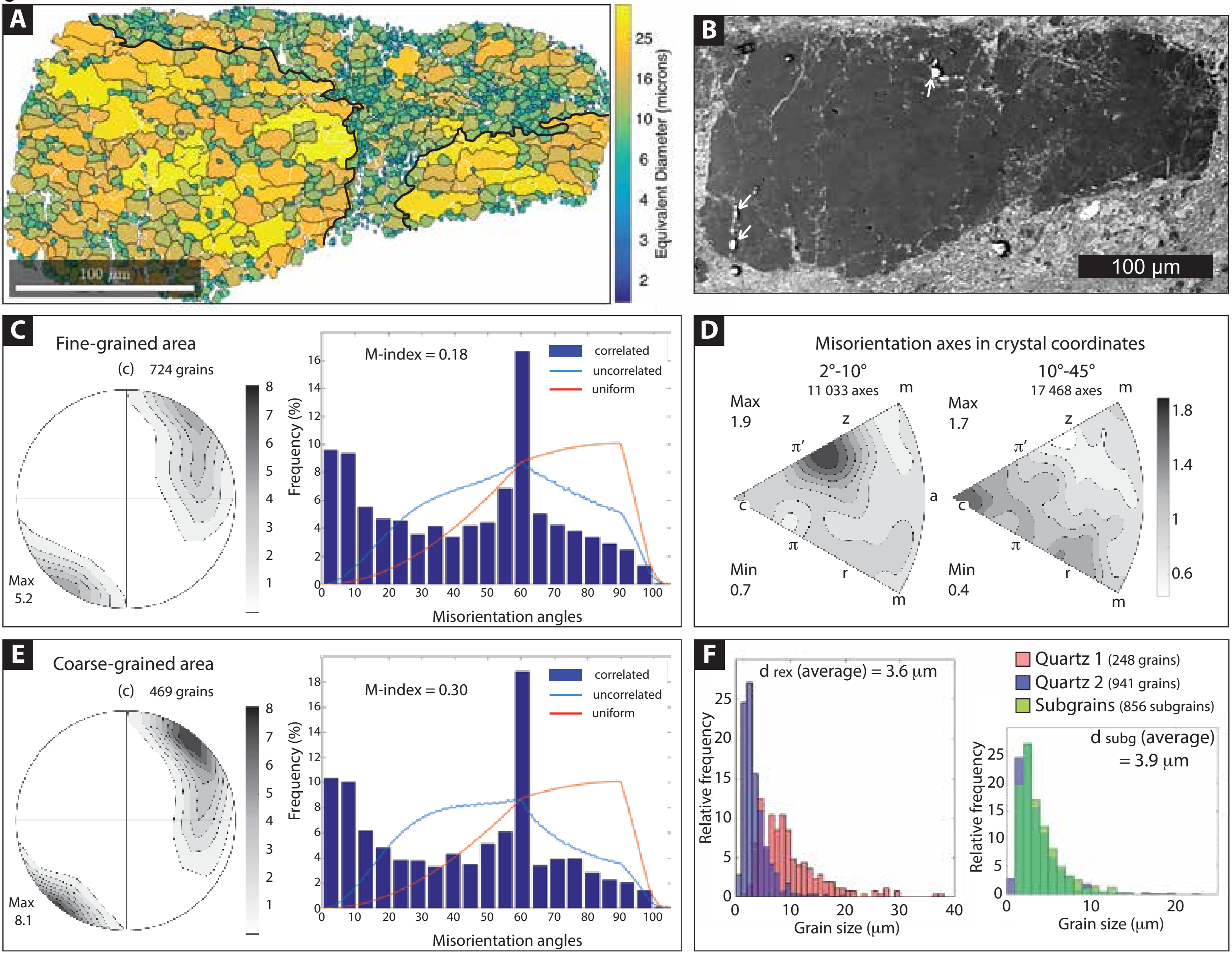
A
100 μm
Equivalent Diameter (microns)
25
16
10
6
4
3
2
B
100 μm
C
Fine-grained area
(c) 724 grains
Max
5.2
M-index = 0.18
correlated
uncorrelated
uniform
Frequency (%)
Misorientation angles
D
Misorientation axes in crystal coordinates
2°-10°
11 033 axes
10°-45°
17 468 axes
Max
1.9
Min
0.7
Max
1.7
Min
0.4
1.8
1.4
1
0.6
E
Coarse-grained area
(c) 469 grains
Max
8.1
M-index = 0.30
correlated
uncorrelated
uniform
Frequency (%)
Misorientation angles
F
d rex (average) = 3.6 μm
Relative frequency
Grain size (μm)
Quartz 1 (248 grains)
Quartz 2 (941 grains)
Subgrains (856 subgrains)
d subg (average)
= 3.9 μm
Relative frequency
Grain size (μm)

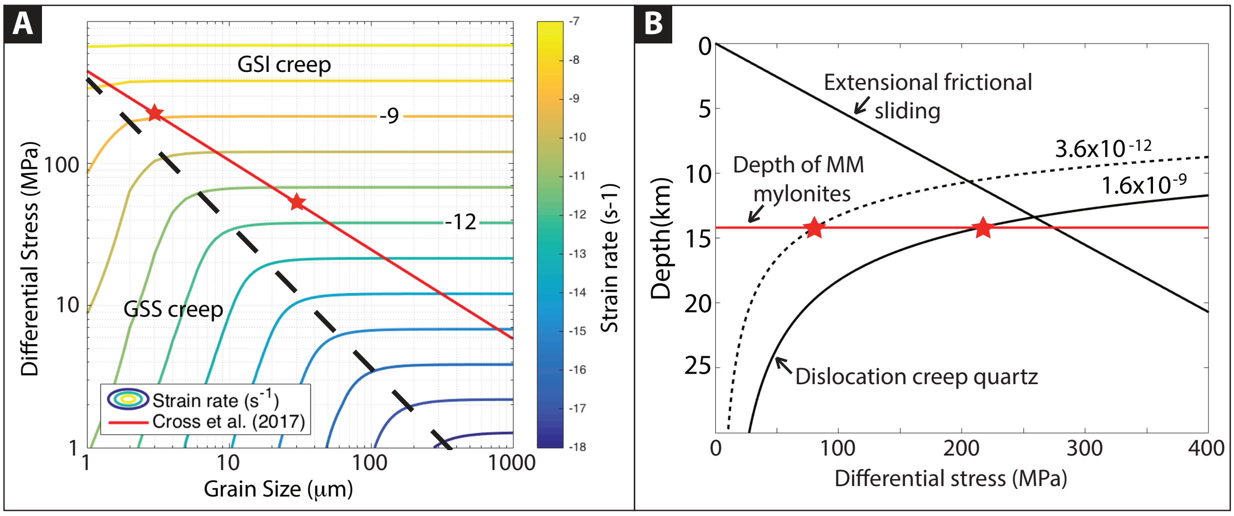

A
GSI creep
-9
-12
GSS creep
Differential Stress (MPa)
Grain Size (μm)
Strain rate (s-1)
Strain rate (s-1)
Cross et al. (2017)
B
Extensional frictional sliding
Depth of MM mylonites
3.6x10-12
1.6x10-9
Dislocation creep quartz
Depth(km)
Differential stress (MPa)

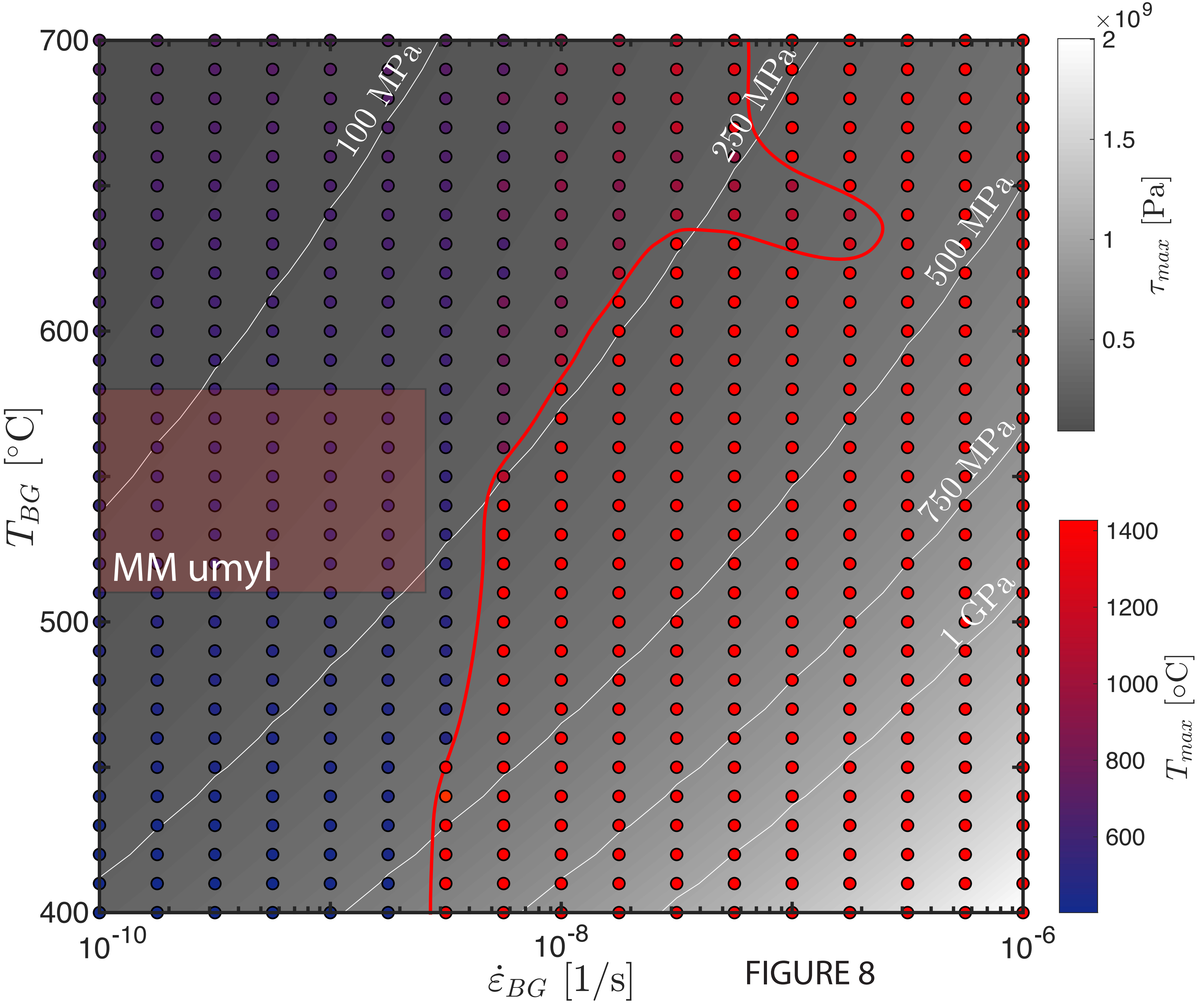

700
600
500
400
T_{BG} [°C]
10^{-10}
10^{-8}
10^{-6}
$\dot{\varepsilon}_{BG}$ [1/s]
100 MPa
250 MPa
500 MPa
750 MPa
1 GPa
MM umyl
$\times 10^9$
2
1.5
1
0.5
τ_{max} [Pa]
1400
1200
1000
800
600
T_{max} [°C]

FIGURE 8